

# A Macrophage–Magnesium Hybrid Biomotor: Fabrication and Characterization

Fangyu Zhang, Rodolfo Mundaca-Uribe, Hua Gong, Berta Esteban-Fernández de Ávila, Mara Beltrán-Gastélum, Emil Karshalev, Amir Nourhani, Yao Tong, Bryan Nguyen, Mathieu Gallot, Yue Zhang, Liangfang Zhang,\* and Joseph Wang\*

**Magnesium (Mg)-based micromotors are combined with live macrophage (MΦ) cells to create a unique MΦ–Mg biohybrid motor system. The resulting biomotors possess rapid propulsion ability stemming from the Mg micromotors and the biological functions provided by the live MΦ cell. To prepare the biohybrid motors, Mg microparticles coated with titanium dioxide and poly(L-lysine) (PLL) layers are incubated with live MΦs at low temperature. The formation of such biohybrid motors depends on the relative size of the MΦs and Mg particles, with the MΦ swallowing up Mg particles smaller than 5 μm. The experimental results and numerical simulations demonstrate that the motion of MΦ–Mg motors is determined by the size of the Mg micro-motor core and the position of the MΦ during the attachment process. The MΦ–Mg motors also perform biological functions related to free MΦs such as endotoxin neutralization. Cell membrane staining and toxin neutralization studies confirm that the MΦs maintain their viability and functionality (e.g., endotoxin neutralization) after binding to the Mg micromotors. This new MΦ–Mg motor design can be expanded to different types of living cells to fulfill diverse biological tasks.**

The development of artificial micromotors that can convert energy to movement and forces has recently become a fascinating research area.<sup>[1–3]</sup> Improvements in the biocompatibility of the micromotor's materials have allowed them to perform some biomedical tasks, such as targeted drug delivery, precise surgery, biosensing, or toxin removal.<sup>[4–6]</sup> Among the different types of biocompatible micromotors, Mg-based Janus micromotors offer distinct advantages for in vivo applications owing to their autonomous propulsion in body fluids including gastric and intestinal fluids, cargo transport and release, and their transient biodegradability properties.<sup>[7–9]</sup> In recent years, Mg-based micromotors have thus been applied in a variety of biomedical applications, such as site-specific gastrointestinal

tract delivery<sup>[10]</sup> in vivo drug or antigen delivery,<sup>[11,12]</sup> and collective and dynamic gastric delivery via micromotor pills.<sup>[13]</sup> While Mg micromotors have been widely tested for dynamic in vivo delivery applications, their ability to manipulate, carry, and transport living cells has not been explored.

Along the line of micromotor design, significant progress has been made recently toward creating biohybrid micro-motors that combine cellular components and synthetic micro/nanoscale materials. Such cell-based micromotors offer considerable promise for diverse in vivo biomedical applications owing to their biocompatibility and biological functionality of the cellular component.<sup>[14]</sup> Live cells can thus be integrated with artificial substrates to produce functional biohybrid devices that possess new and improved capabilities. Such cell-based micromotors can be classified in two types. The first one relies

on the intrinsic motility of live cells, such as spermatozoa,<sup>[15]</sup> bacteria,<sup>[16]</sup> and cardiomyocytes,<sup>[17]</sup> for transporting artificial material payloads. The microorganisms thus act as engines to form active biohybrid swimming systems powered by cellular actuation. The second type consists of cell-based materials, such as cell membranes, and synthetic micromotors that provide the motion. Such combination of micromotors with cell components confers the micromotor with cell-like properties<sup>[18,19]</sup> and improved biofunctionality.<sup>[20]</sup> Besides cell membrane-coated micromotors, various types of cells have also been used in biomedical applications due to their large drug loading capacity,<sup>[21]</sup> natural homing tendency toward inflammation sites,<sup>[22]</sup> and easy genetic engineering for gene delivery.<sup>[23]</sup> The combination of intact cells and engineered motors has resulted in several cell-based biohybrid micromotor designs for diverse applications, including stem cell-based motors for drug delivery,<sup>[24]</sup> red blood cell-motors for on-demand cargo delivery,<sup>[25]</sup> and NIH 3T3 cell-based motors for precise control and patterning.<sup>[26]</sup> Although such cell-based motors have demonstrated clear advantages as drug delivery carriers, it will be particularly interesting to explore the possibility of integrating intact live cells with biocompatible and biodegradable artificial micromotors, such as the Mg-based micromotors, to form a biohybrid motor system, which can potentially be applied for in vivo operations.

F. Zhang, R. Mundaca-Uribe, Dr. H. Gong, Dr. B. Esteban-Fernández de Ávila, Dr. M. Beltrán-Gastélum, E. Karshalev, Dr. A. Nourhani, Y. Tong, B. Nguyen, M. Gallot, Y. Zhang, Prof. L. Zhang, Prof. J. Wang  
Department of Nanoengineering  
University of California San Diego  
La Jolla, CA 92093, USA  
E-mail: zhang@ucsd.edu; josephwang@ucsd.edu

 The ORCID identification number(s) for the author(s) of this article can be found under <https://doi.org/10.1002/adma.201901828>.

DOI: 10.1002/adma.201901828

Herein, we present a new approach, combining living macrophage (MΦ) cells with Mg micromotors to prepare MΦ–Mg hybrid motors, which possess the powerful propulsion of the Mg micromotors and preserve the biological function of the cells. As a critical cell in the innate immune system, MΦs play a major role in the regulation of homeostasis,<sup>[27]</sup> can swallow and digest pathogens,<sup>[28]</sup> and have specific receptors for bio-toxins such as endotoxins.<sup>[29]</sup> The new biohybrid micromotors are fabricated by coating Mg microparticles with titanium dioxide ( $\text{TiO}_2$ ) and a poly(L-lysine) (PLL) layer, and attaching the MΦ to the outer PLL coating via electrostatic interactions. The resulting MΦ–Mg biohybrid motors maintain the functionality and viability of MΦ cells and offer efficient transport of the living cells. Numerical modeling of the propulsion dynamics of the resulting MΦ–Mg dimer motor is in good agreement with the experimental observations. In addition, the viability and biological function of the attached MΦ are retained and the cell can bind and neutralize pathogenic toxins, such as endotoxins. Overall, this work presents an attractive method to fabricate a biohybrid micromotor, consisting of whole cells attached onto autonomously propelled synthetic micromotors. While the new biohybrid strategy is demonstrated here using MΦs as model living cells, it could be readily expanded to other types of cells that possess different functionalities.

The new biohybrid strategy for moving whole living cells in biological media consists of utilizing a synthetic Mg-based micromotor while retaining the viability, integrity, and function of the cells. We used MΦ as a model living cell owing to its

critical role as an immune cell. The design of the new biohybrid motor relies on the attachment of MΦs to Mg micromotors via electrostatic attraction between the negatively charged cell membrane and the positively charged outer PLL coating on the Mg micromotor. Such interaction ensures that the open area of the Mg micromotor remains exposed to the biological fluid for efficient bubble propulsion. The fabrication protocol, illustrated in Figure 1A, consists of modifying Mg/ $\text{TiO}_2$  micromotors (commonly  $\approx 20 \mu\text{m}$  size) with 0.01% PLL coating over a glass slide (Figure 1A, steps 1 and 2). Subsequently, the PLL-modified Mg micromotors and MΦs were suspended in Dulbecco's modified eagle medium (DMEM) and incubated for 1 h at  $4^\circ\text{C}$  (Figure 1A, step 3). It should be noted that the MΦs remained stable on the PLL motor surface after longer times (Figure S1, Supporting Information). After the incubation, the MΦ–Mg motors were washed to eliminate all the unbound cells. Subsequently, the MΦ–Mg motors were released and placed in an acidic environment, where the motors propelled spontaneously due to the reaction between the Mg core and the protons present in the acidic fluid, which generates a hydrogen bubble tail and propulsion thrust (Figure 1A, step 4).

Figure 1B (left side) shows a scanning electron microscopy (SEM) image of a MΦ–Mg motor, displaying the binding between a MΦ cell and a Mg micromotor (pseudocolored in pink and green, respectively) with its opening exposed to ambient medium. Energy-dispersive X-ray spectroscopy (EDX) images illustrate the presence and elemental distribution of Mg and Ti within the micromotor structure (Figure 1B, right).

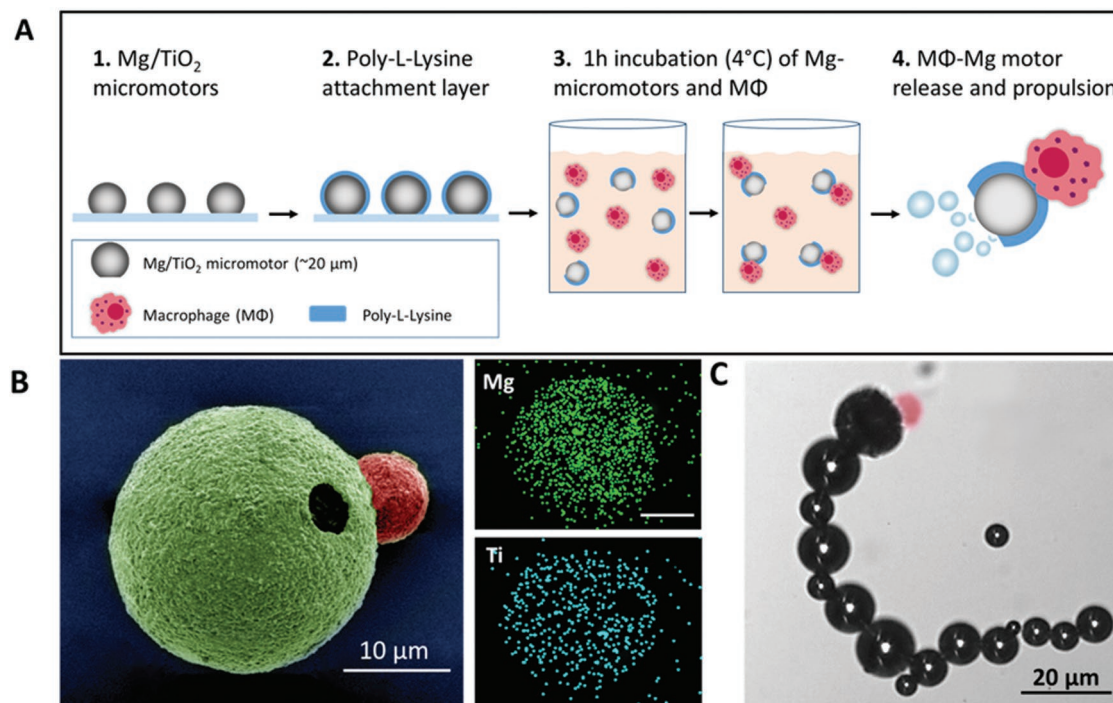


**Figure 1.** MΦ–Mg micromotor preparation and structural characterization. A) Schematic of the preparation of the MΦ–Mg motor: 1) ALD of  $\text{TiO}_2$  over Mg microparticles; 2) Deposition of a PLL layer over the Mg/ $\text{TiO}_2$  micromotors; 3) Incubation of Mg-micromotors and MΦs for 1 h at  $4^\circ\text{C}$ ; 4) MΦ–Mg motor release and propulsion in simulated gastric fluid (pH 1.3). B) Left: SEM image of a MΦ–Mg motor (Mg-micromotor is pseudocolored in green and MΦ is pseudocolored in pink); Right: EDX images showing the distribution of elemental Mg (green) and Ti (cyan). C) Microscopy image (corresponding to Video S1 in the Supporting Information) displaying the motion of a MΦ–Mg motor in gastric fluid simulant (pH 1.3); the MΦ is pseudocolored in pink).

The aperture observed in the Ti mapping image corresponds to the opening in the  $\text{TiO}_2$  shell produced during the atomic layer deposition (ALD) process. The motion of the  $\text{M}\Phi\text{-Mg}$  motors was evaluated using simulated gastric fluid ( $\text{pH} 1.3$ ), which led to the generation of hydrogen bubbles and corresponding thrust. Figure 1C displays a microscopy image of a  $\text{M}\Phi\text{-Mg}$  motor moving in simulated gastric fluid, showing the  $\text{M}\Phi$  (pseudocolored in pink) attached to the Mg micromotor, along with the corresponding hydrogen bubble tail. The  $\text{M}\Phi\text{-Mg}$  motors displayed a lifetime of  $\approx 5$  min, characteristic of the gradual Mg depletion,<sup>[13]</sup> with an average speed of  $127.3 \mu\text{m s}^{-1}$ . It should be noted that the  $\text{M}\Phi$  cells remained attached firmly to the  $\text{M}\Phi\text{-Mg}$  motors throughout these experiments, as illustrated in the corresponding Video S1 in the Supporting Information, reflecting their strong binding to the PLL motor layer.

The propulsion characteristics of the resulting  $\text{M}\Phi\text{-Mg}$  motors were evaluated in vitro in simulated gastric acid. The schematic and the microscopy images shown in Figure 2A (captured from Video S2 in the Supporting Information, at 0, 1, and 3 min) display the movement of  $\text{M}\Phi\text{-Mg}$  motors with a motor diameter of: i)  $20\text{--}25 \mu\text{m}$  or ii)  $10\text{--}15 \mu\text{m}$ . Efficient hydrogen bubble generation propelled the Mg micromotor and  $\text{M}\Phi\text{-Mg}$  motor in simulated gastric fluid (Figure 2B and microscopy images at 1 min). Once the Mg motor core was dissolved fully (i.e., completion of the Mg-proton reaction), only open  $\text{TiO}_2$  shells remained (Figure 2C), and the propulsion was halted while the  $\text{M}\Phi$  remained attached to the resulting shell (images at 3 min).

Figure 2D schematically illustrates the biohybrid structure with the  $\text{M}\Phi$  attached to the Mg microparticle. The motion behavior of the  $\text{M}\Phi\text{-Mg}$  motor primarily depends on the dynamic characteristics of the biohybrid micromotor, the position of the  $\text{M}\Phi$  on the Mg microparticle and the ratio of the effective radius of the  $\text{M}\Phi$   $R_{\text{M}\Phi}$  to the Mg microparticle radius  $R_{\text{Mg}}$ , defined by:

$$\lambda = \frac{R_{\text{M}\Phi}}{R_{\text{Mg}}} = \frac{d_{\text{M}\Phi}}{d_{\text{Mg}}} \quad (1)$$

where  $d_{\text{M}\Phi}$  and  $d_{\text{Mg}}$  are the effective diameters of  $\text{M}\Phi$  and Mg microparticle, respectively.

For a typical  $\text{M}\Phi\text{-Mg}$  dimer motor of length  $l \approx 30 \mu\text{m}$ , moving with speed  $v \approx 100 \mu\text{m s}^{-1}$  in a fluid of density  $\rho \approx 1000 \text{ kg m}^{-3}$  and viscosity  $\mu \approx 8.9 \times 10^{-4} \text{ Pa s}$ , the Reynolds number is  $Re = \rho lv/\mu \approx 0.003 \ll 1$ . In the low Reynolds number regime, the fluid flow is governed by Stokes equation and the  $\text{M}\Phi\text{-Mg}$  dimer motor velocity is linearly proportional to the force exerted on the motor. Approximating the Mg microparticle and  $\text{M}\Phi$  as spheres, and employing a zeroth-order approximation by adding up the hydrodynamics effect of the spherical particles independently, the speed of the  $\text{M}\Phi\text{-Mg}$  motor  $v_{\text{dimer}}$  relates to the speed of the bare Mg micromotor  $v_{\text{Mg}}$  by

$$v_{\text{dimer}} = \frac{1}{1 + \lambda} v_{\text{Mg}} \quad (2)$$

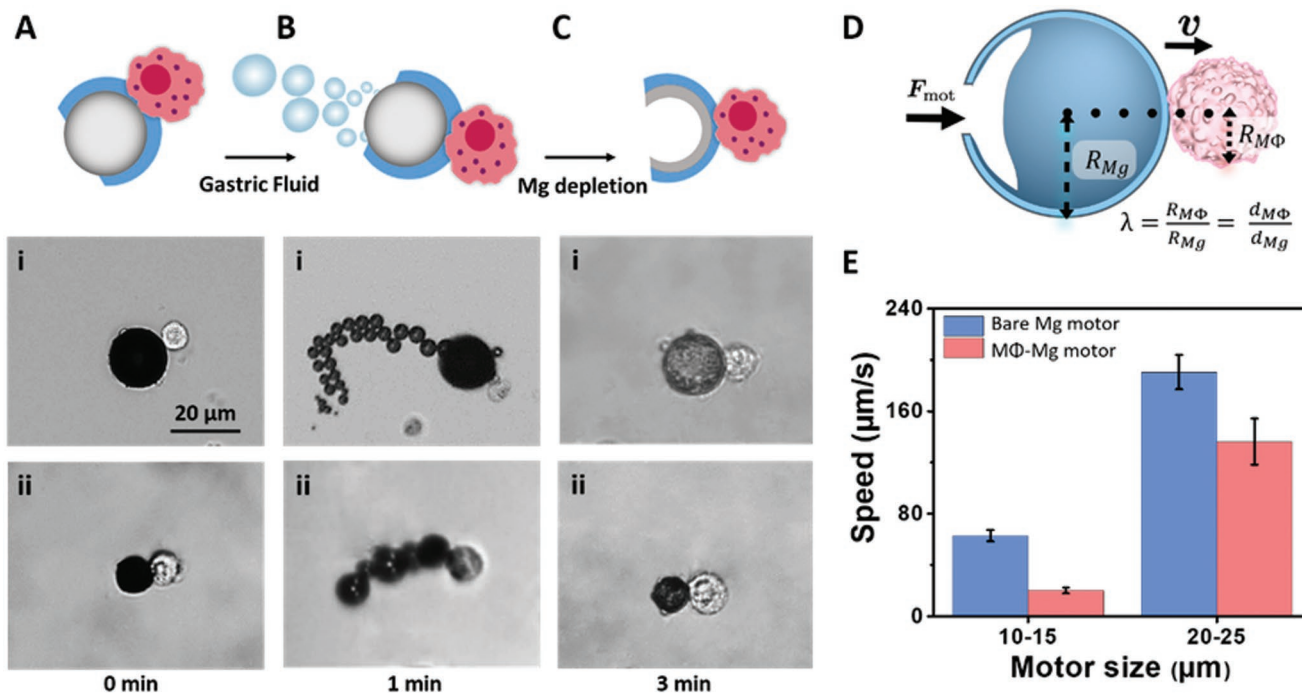


**Figure 2.** Propulsion characteristics of  $\text{M}\Phi\text{-Mg}$  motors. A) Schematic and microscopy images of a  $\text{M}\Phi\text{-Mg}$  micromotor with motor diameters of: i)  $20\text{--}25 \mu\text{m}$  or ii)  $10\text{--}15 \mu\text{m}$  at time = 0 min. B) Schematic and microscopy images of a  $\text{M}\Phi\text{-Mg}$  micromotor with motor diameters of: i)  $20\text{--}25 \mu\text{m}$  or ii)  $10\text{--}15 \mu\text{m}$  propelling in gastric fluid solutions at time = 1 min. C) Schematic of the  $\text{M}\Phi\text{-Mg}$  shell (with partial Mg depletion) at time = 3 min, along with microscopy images of a  $\text{M}\Phi\text{-Mg}$  shell corresponding to the two motor sizes (i, ii) at time = 3 min. D) Modeling of the dynamics of a dimer where a  $\text{M}\Phi$  of an effective radius  $R_{\text{M}\Phi}$  is attached to a Mg-based micromotor with radius of  $R_{\text{Mg}}$  (following partial Mg depletion). E) Comparison of the speed of  $10\text{--}15 \mu\text{m}$  and  $20\text{--}25 \mu\text{m}$  Mg motors and  $\text{M}\Phi\text{-Mg}$  motors in the gastric fluid simulant (values defined at time = 1 min).

where the relative size  $\lambda = d_{\text{M}\Phi} / d_{\text{Mg}}$  is the ratio of the effective diameter of the MΦ,  $d_{\text{M}\Phi}$  to the Mg diameter  $d_{\text{Mg}}$ . In the limit of a very large MΦ compared to the Mg microparticle ( $\lambda \gg 1$ ), the micromotor's driving force is not strong enough to effectively move the MΦ. Practically, in this regime the MΦ engulfs the micromotor and there will be no motion. On the other hand, for very large micromotors ( $\lambda \ll 1$ ) the MΦ-Mg motor moves with a speed close to that of the bare Mg micromotor. Our experimental regime is between these two extremes.

To compare the modeling prediction with experimental results, we averaged the MΦ-Mg motor velocity and their Mg micromotor and MΦ radii for dimers with the micromotor diameter in the range of 23–44  $\mu\text{m}$  from the experimental data. We obtained an average velocity of  $v_{\text{dimer}} \approx 127.3 \pm 6.1 \mu\text{m s}^{-1}$ , and average diameters for bare Mg micromotor  $d_{\text{Mg}} \approx 33 \mu\text{m}$ , and  $d_{\text{M}\Phi} \approx 10.6 \mu\text{m}$  ( $\lambda \approx 0.32$ ). To compare our model with the experimental data, we fitted first a linear regression for bare Mg micromotors as a function of their velocities. For diameter  $d_{\text{Mg}} = 33 \mu\text{m}$  the linear fit gives a value of  $v_{\text{Mg}} = 167 \mu\text{m s}^{-1}$  for bare Mg micromotor velocity. Plugging this value in Equation (2) along with  $\lambda = 0.32$ , our model approximates a dimer velocity to be  $v_{\text{dimer}} = 126.5 \mu\text{m s}^{-1}$ , which is very close to the experimental velocity value ( $v_{\text{dimer}} = 127.3 \pm 6.1 \mu\text{m s}^{-1}$ ). The model can qualitatively explain the behavior of the dimers due

to the nature of the zeroth order approximation. A good agreement is observed between the model and the experimental data despite the approximation of Mg microparticle and MΦ as perfect spheres and the fluctuations in the experimental data.

The experimental average speed for bare Mg micromotors in the range of 20–25  $\mu\text{m}$  and 10–15  $\mu\text{m}$  in simulated gastric fluid was measured, obtaining values of  $190.5 \pm 13.24$  and  $62.8 \pm 4.3 \mu\text{m s}^{-1}$ , respectively, and were compared to the speed of MΦ-Mg motors at 1 min time, with average speeds of  $136.3 \pm 17.9$  and  $19.9 \pm 2.1 \mu\text{m s}^{-1}$ , respectively (Figure 2E). The corresponding theoretical values from Equation (2) for a MΦ-Mg motor with MΦ of diameter  $d_{\text{M}\Phi} = 15 \mu\text{m}$  are  $114.294$  and  $28.545 \mu\text{m s}^{-1}$  using Mg micromotors of 20–25 and 10–15  $\mu\text{m}$ , respectively. The observed MΦ-Mg motor velocities correspond to a relative speed of about five body lengths per second, indicating that these biohybrid motors can rapidly react and move in the gastric fluid. In addition, no propulsion movement was observed when the MΦs were attached to 5  $\mu\text{m}$  Mg micromotors.

Since the MΦ-Mg biohybrid motor design is based on the interaction between MΦs and Mg micromotors, it is essential to verify that these cells do not engulf the motors after the binding process. Few studies have examined the relation between the particle size and its engulfment by MΦ.<sup>[30]</sup> In this

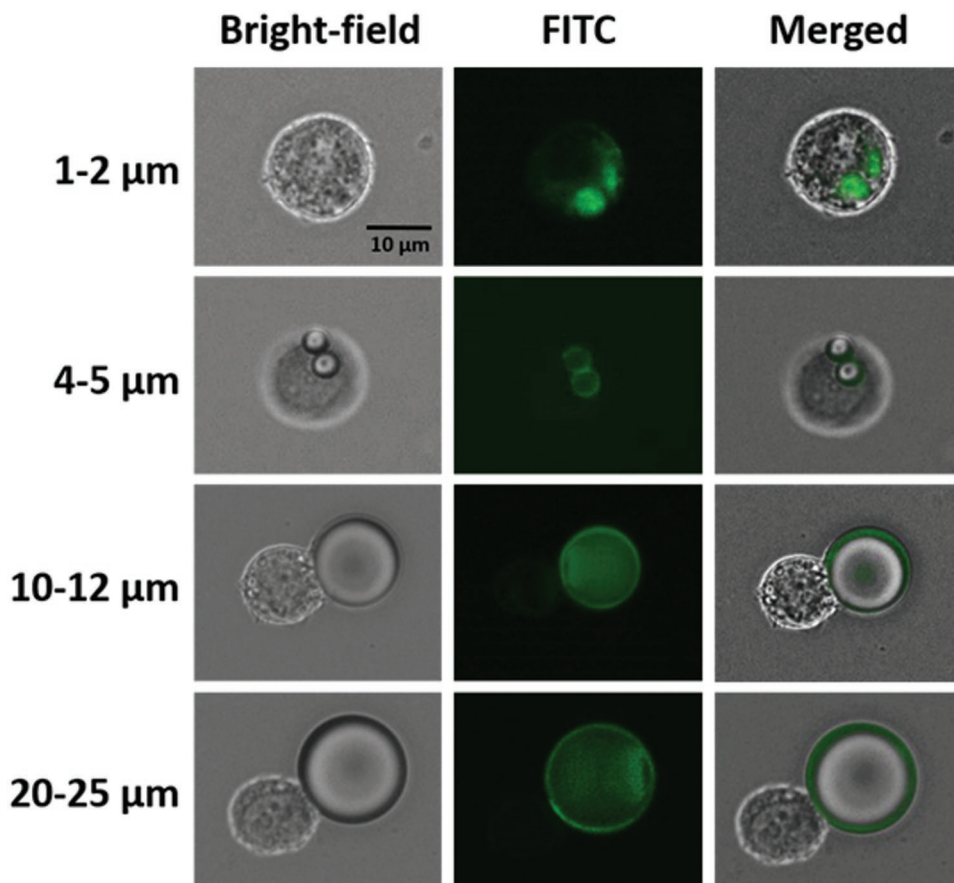


**Figure 3.** Size-dependent interaction of MΦs with polystyrene (PS) microparticles. For fluorescence imaging, the PS particles were labeled with FITC dye (green color). Small PS particles ( $<10 \mu\text{m}$ ) were prone to be engulfed by the MΦ while large particles attached on the cell membrane of the MΦ (not internalized).

work, we studied the size-dependent engulfment by MΦs using polystyrene (PS) microparticles with four different size ranges (1–2, 4–5, 10–12, and 20–25  $\mu\text{m}$ ) as model particles in the size range of the Mg micromotors. **Figure 3** displays bright-field, fluorescence (green channel, FITC dye), and merged images corresponding to MΦs incubated with the different sized PS microparticles. It is observed that the 1–2 and 4–5  $\mu\text{m}$  PS microparticles were internalized by the MΦs, while the bigger PS microparticles (10–12, and 20–25  $\mu\text{m}$ ) just interacted with the outer membrane of the MΦs without being internalized. These results not only explain why no propulsion was observed using Mg micromotors smaller than 5  $\mu\text{m}$ , but also indicate that Mg micromotors larger than 5  $\mu\text{m}$  are essential for realizing MΦ–Mg biohybrid motors.

Another important factor to consider in the fabrication of the MΦ–Mg motors is the cell viability and functionality of MΦ cells following the different modification steps. To test these, Calcein AM ( $\lambda_{\text{ex}}/\lambda_{\text{em}}$ , 488 and 520 nm, respectively) and lipopolysaccharide (LPS) conjugated with Alexa Fluor594 ( $\lambda_{\text{ex}}/\lambda_{\text{em}}$ , 590 and 617 nm, respectively) were used to evaluate the cell viability and functionality, respectively. **Figure 4** demonstrates that the MΦ attached to the micromotor showed a strong green fluorescence, which is consistent with the free MΦ, and indicates that the motor conjugation process does not affect the cell viability. In addition, the LPS binding capability of the MΦ was mostly retained after the modification process, as the MΦ conjugated with the motor showed comparable fluorescence intensity after incubating with LPS conjugates. Further studies were performed to evaluate the viability of the attached MΦs after the micromotor reaction in gastric fluid simulant. The results (shown in Figure S3 in the Supporting Information) demonstrate that the MΦs remained viable, retaining all their biological functions after being exposed to gastric fluid for 5 min, 1 h, 2 h, and 4 h, confirming the good

stability of the system. Overall, these results demonstrate that the motor conjugation process does not affect either the cell viability or the membrane functional proteins, and that the attached MΦ is not damaged due to the hybrid biomotor fabrication process.

As was stated before, it is essential that the MΦs maintain their viability and biological functionality after binding to the Mg micromotors. Specifically, MΦs have the ability to bind and neutralize endotoxins. LPS is a hazardous endotoxin released from the membrane of Gram-negative bacteria, which can induce strong inflammatory response<sup>[31]</sup> and has a preponderant role in the development of sepsis.<sup>[32,33]</sup> Since this is one of the most important roles of MΦs in the body, it is critical to ensure that these cells are still functional and retain their endotoxin binding ability. **Figure 5A** illustrates an active MΦ–Mg motor binding to the endotoxin released by *Escherichia coli*. Aiming to test the ability of the MΦ–Mg motor to neutralize LPS, to illustrate the cell functionality after its binding with the Mg micromotors, we thus performed in vitro LPS binding and neutralization experiments. For this study, 0.25 EU (units of endotoxin) were used for each group. First, the maximum LPS binding capacity of a fixed amount of MΦs ( $1 \times 10^6$ ) was examined by titrating the concentration of LPS, finding that  $1 \times 10^6$  MΦs can neutralize 0.25 EU LPS after 1 h incubation with periodic shaking. Then, the LPS binding ability of MΦ–Mg motors was compared to that of free MΦs (used as a positive control). In addition, DMEM medium was used as a negative control. After incubation, remaining LPS quantification was carried out using ToxinSensor chromogenic LAL endotoxin assay kit following the manufacturer's guideline. The results showed that following 5 min reaction, the MΦ–Mg motors removed  $66.82 \pm 6.31\%$  of LPS from the system, around 13% more than free MΦs ( $53.34 \pm 4.48\%$ ). For a better understanding, these data are graphed in **Figure 5B** in terms of remaining LPS, where the lowest value is obtained with the

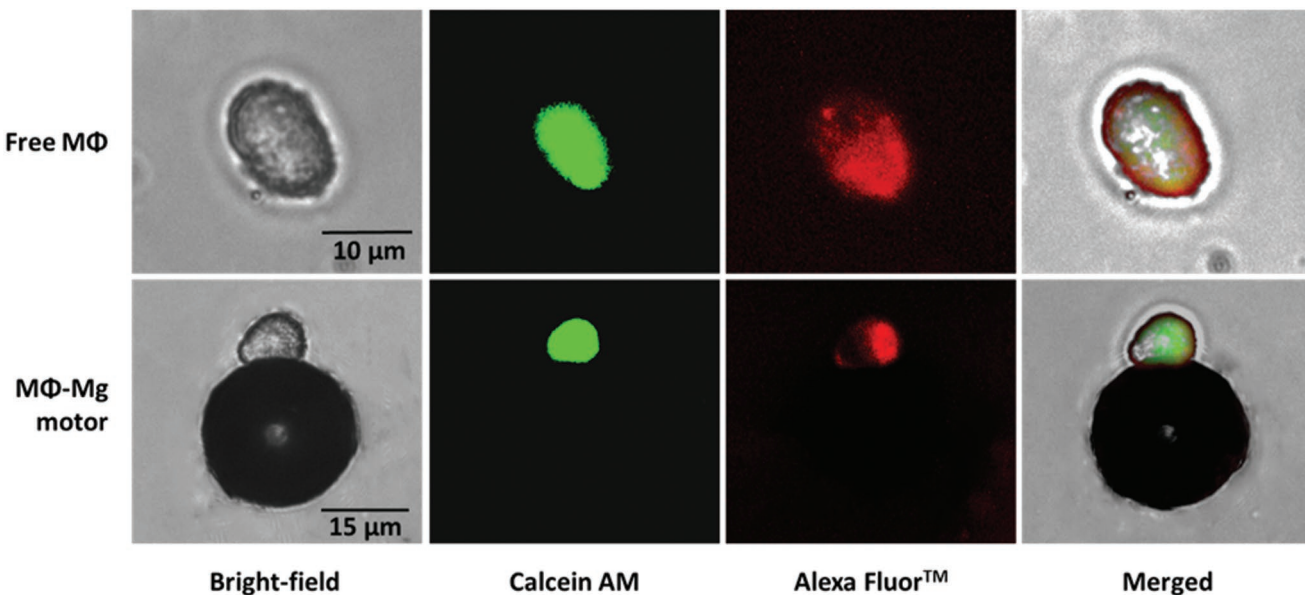


**Figure 4.** Cell viability and functionality of a free MΦ and a MΦ attached to a Mg motor. Microscopy images of a free MΦ (top) and a MΦ–Mg motor (bottom) after 30 min incubation with Calcein AM ( $\lambda_{\text{ex}}/\lambda_{\text{em}}$ , 488 and 520 nm) and LPS labeled with Alexa Fluor594 ( $\lambda_{\text{ex}}/\lambda_{\text{em}}$ , 590 and 617 nm), in DMEM medium at 37 °C.

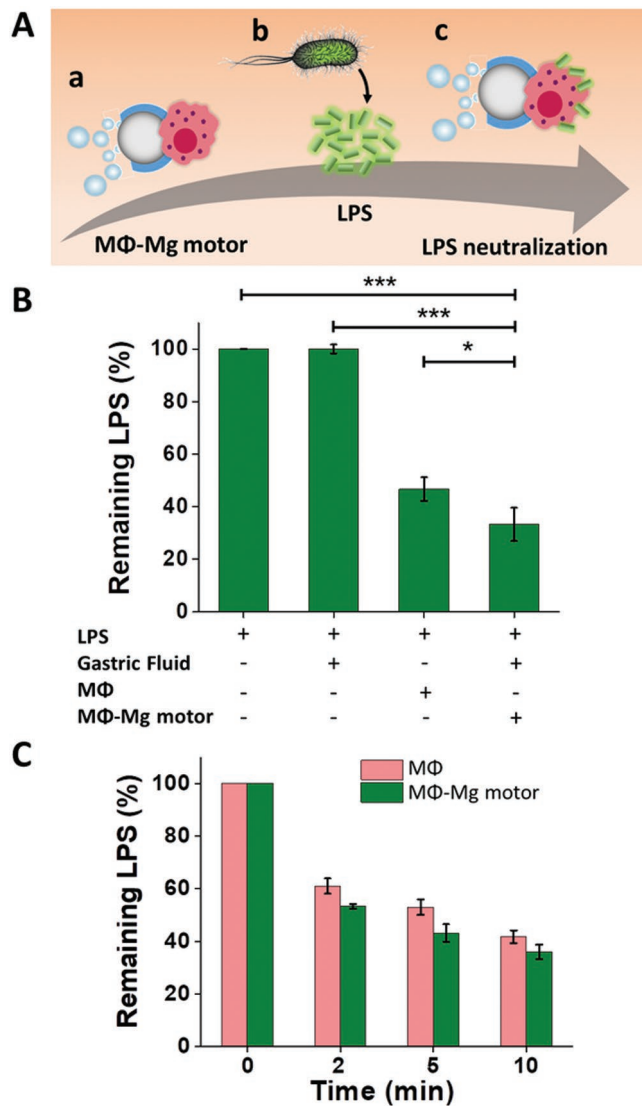


**Figure 5.** Endotoxin (LPS) neutralization with MΦ–Mg motors. A) Schematic illustration of using MΦ–Mg motors to neutralize LPS produced by bacteria: a) MΦ–Mg motors propelling in a bacterial culture medium; b) LPS released by *E. coli* bacteria; c) LPS neutralization by MΦ–Mg motors. B) LPS removal with MΦ–Mg motors in comparison with free MΦs. Error bars estimated as a triple of SD ( $n = 3$ ). Bars represent median values. \* $P < 0.05$ , \*\*\* $P < 0.001$ . C) Evaluation of MΦ–Mg motor toxin neutralization performance at different times and comparison with free MΦs.

MΦ–Mg motors as demonstrated by the statistical analysis. This can be explained by the fact that using the MΦ–Mg motors, the MΦ receptor is rapidly moving through the solution, keeping the reaction under constant stirring and thus binding more LPS, while the free MΦs are present in suspension. These results illustrate that this new biohybrid motor maintains the natural biological function of MΦs.

To gain insights into the characterization of this new biohybrid motor, a time-dependence study was carried out, in which the performance of the MΦ–Mg motors and the free MΦs toward binding LPS at different time points was evaluated

(Figure 5C). After 2 min of reaction, MΦ–Mg motors neutralized nearly 45% of the LPS, after 5 min almost a 56%, and after 10 min around 66%. Since the micromotor velocity tends to be higher during the initial 2 min, the best performance of this new biohybrid is expected during this period, which is consistent with the obtained data.

We have reported the fabrication and unique property of a biohybrid MΦ–Mg motor, combining a Mg-based micromotor with a living MΦ cell. The resulting MΦ–Mg motors were able to propel in acidic environment, reaching average speeds of  $127.3 \mu\text{m s}^{-1}$ , which was in agreement with numerical modeling based on dynamic characteristics of the micromotor, such as its relative size and position of the MΦ on the micromotor. The formation of the MΦ–Mg motors is dependent on the size of the Mg micromotors; larger than  $10 \mu\text{m}$  Mg micromotors resulted in MΦs attaching to the motor surface, but smaller than  $5 \mu\text{m}$  Mg micromotors would be engulfed by the MΦs. The propulsion behavior of the Mg micromotors enabled movement of the whole MΦ–Mg motors and thus rapid transport of the attached MΦs, while retaining the viability and biological functionality of their source cells, as indicated from the endotoxin neutralization study. While MΦs were used in this work, the new biohybrid strategy represents a platform technology and should be generalizable to other types of cells for other specific application purposes.

## Experimental Section

**Mg Micromotors Fabrication:** Mg-based micromotors were prepared using commercial magnesium (Mg) microparticles (catalog #FMW20, TangShan WeiHao Magnesium Powder Co.; average size, 20 and  $10 \mu\text{m}$ ) as the core. The Mg microparticles were initially washed with acetone to remove impurities. After drying under  $\text{N}_2$  flow the Mg microparticles were dispersed onto glass slides (2 mg of Mg microparticles per glass slide) and coated with TiO<sub>2</sub> by ALD (at  $100^\circ\text{C}$  for 3000 cycles) using a Beneq TFS 200 atomic layer deposition system. This deposition allowed for leaving a small opening at the contact point of the particle to the surface of the glass slide.

**MΦ–Mg Motor Fabrication:** To fabricate the MΦ–Mg motor, the Mg micromotors were coated with  $100 \mu\text{L}$  of 0.01% (w/v) PLL solution prepared in water (Sigma-Aldrich, P8920) to allow for better binding to the MΦs. This PLL coating was distributed around 80% of the surface of the Mg micromotor, thus facilitating later interactions with MΦs at 1:1 ratio. J774.A1 mouse MΦs (diameter in suspension, 10–16  $\mu\text{m}$ ) were purchased from the American Type Culture Collection (ATCC). Then, the modified micromotors were collected from the glass slide by gently scratching and washed 2 times with ethanol and Dulbecco's modified Eagle medium (DMEM), with 3 min centrifugation at 3000 rpm between each washing step. Finally, 2 mg of these micromotors and  $1 \text{ mL}$  of MΦs ( $1 \times 10^6$  cells per mL of DMEM) were incubated at  $4^\circ\text{C}$  for 1 h to allow the attachment of MΦs with Mg motors to form MΦ–Mg motors. Subsequently, the MΦ–Mg motors were washed three times with DMEM to remove all the unbound cells.

**MΦ–Mg Motor Characterization:** Bright-field, fluorescence, and merged images of the MΦ–Mg motors were obtained with an EVOS FL microscope coupled with 20 $\times$  and 40 $\times$  objectives and a fluorescence filter for green light excitation. Scanning electron microscopy (SEM) images were captured using a FEI Quanta 250 ESEM instrument (Hillsboro, Oregon, USA), using an acceleration voltage of 10 kV. Energy-Dispersive X-Ray Spectroscopy (EDX) mapping analysis was carried out with an Oxford EDS detector attached to SEM instrument and controlled by Pathfinder software.

**MΦ–Mg Motor Propulsion:** The MΦ–Mg motor propulsion was evaluated using simulated gastric fluid (Sigma-Aldrich, 0 1651), which was diluted 10 times and supplemented with 0.2% Triton X-100 (Fisher

Scientific, FairLawn, NJ, USA) as a surfactant. To capture videos of the motion of the MΦ–Mg motor, an inverted optical microscope (Nikon Eclipse Instrument Inc. Ti-S/L100) coupled with different microscope objectives (10×, 20×, and 40×), a Hamamatsu digital camera C11440, and NIS Elements AR 3.2 software was used. An NIS Element tracking module was used to measure the speed.

**MΦ-Particle Interaction Study:** Polystyrene (PS) particles were washed two times with ethanol through centrifugation at 3000 rpm for 3 min each; then the microparticles were transferred to DMEM medium, washed two times with this medium, and incubated in a 0.01% PLL solution which was labeled with the fluorescein (FITC) dye for visualization. The PS microparticles and MΦs were incubated in DMEM for 1 h at 4 °C and observed under the optical and fluorescence microscope.

**MΦ Viability and Functionality Study:** Calcein AM ( $\lambda_{\text{ex}}/\lambda_{\text{em}}$ , 488/520 nm, respectively) (ThermoFisher Scientific, C3100 MP), Lipopolysaccharides from *Escherichia coli* Serotype 055:B5, and Alexa Fluor 594 conjugates ( $\lambda_{\text{ex}}/\lambda_{\text{em}}$ , 590/617 nm, respectively) (ThermoFisher Scientific, L23353) were used to study cell viability and LPS binding functionality simultaneously. In the study, 2 mg of MΦs-Mg motors,  $3 \times 10^{-6}$  M of Calcein AM, and 1 EU mL<sup>-1</sup> of LPS conjugate with alexa fluor were incubated at 37 °C for 30 min in DMEM, homogenizing every 5 min; then, free cells and MΦs-Mg motors were analyzed using an EVOS FL microscope coupled with 20× and 40× microscopes objectives and fluorescence filters for green and red light excitation. Calcein AM was used for studying the MΦ viability after reaction and propulsion in gastric fluid simulant. The MΦ–Mg motors were exposed to the gastric fluid simulant during different times. Then, MΦ–Mg motors were incubated with Calcein AM at 37 °C for 30 min and microscopy images were taken to evaluate the cell viability.

**Endotoxin Binding and Neutralization:** To evaluate the in vitro endotoxin (LPS) binding and neutralization, 2 mg of MΦ–Mg motors and 0.25 EU of LPS were left reacting in acidic medium for 5 min; free MΦs ( $1 \times 10^6$  cell per mL) were used as positive control and DMEM as negative control. After the reaction was completed, the sample was centrifuged at 1400 rpm for 3 min to spin down the cells together with the Mg micromotors. To quantify LPS in the supernatant, the Toxisensor chromogenic LAL endotoxin assay kit (Cat. No. L00350) was used. The binding and neutralization capacity of the MΦ–Mg motor was calculated by deducting the remaining LPS in the supernatant.

## Supporting Information

Supporting Information is available from the Wiley Online Library or from the author.

## Acknowledgements

F.Z., R.M.-U., and H.G. contributed equally to this work. The manuscript was written through contributions of all authors. All authors have given approval to the final version of the manuscript. This work was supported by the Defense Threat Reduction Agency Joint Science and Technology Office for Chemical and Biological Defense (Grant Numbers HDTRA1-18-1-0014, HDTRA1-14-1-0064, and HDTRA1-13-1-0002). R.M-U. acknowledges the support from the Fulbright grants and the CONICYT PFCHA/DOCTORADO BECAS CHILE/2015-56150011. M.B.-G. acknowledges a postdoctoral fellowship from Consejo Nacional de Ciencia y Tecnología (CONACyT). E.K. acknowledges support from the Charles Lee Powell Foundation.

## Conflict of Interest

The authors declare no conflict of interest.

## Keywords

biohybrid, endotoxin, macrophage, micromotor, propulsion

Received: March 22, 2019

Revised: April 15, 2019

Published online:

- [1] H. Wang, M. Pumera, *Chem. Rev.* **2015**, *115*, 8704.
- [2] J. Wang, *Nanomachines: Fundamentals and Applications*, John Wiley & Sons, Weinheim, **2013**.
- [3] X. Z. Chen, M. Hoop, F. Mushtaq, E. Siringil, C. Hu, B. J. Nelson, S. Pane, *Appl. Mater. Today* **2017**, *9*, 37.
- [4] B. Esteban-Fernández de Ávila, P. Angsantikul, D. E. Ramírez-Herrera, F. Soto, H. Teymourian, D. Dehaini, Y. Chen, L. Zhang, J. Wang, *Sci. Rob.* **2018**, *3*, eaat0485.
- [5] F. Mou, C. Chen, Q. Zhong, Y. Yin, H. Ma, J. Guan, *ACS Appl. Mater. Interfaces* **2014**, *6*, 9897.
- [6] J. Li, B. Esteban-Fernández de Ávila, W. Gao, L. Zhang, J. Wang, *Sci. Rob.* **2017**, *2*, eaam6431.
- [7] Z. Wu, T. Li, W. Gao, T. Xu, B. Jurado-Sánchez, J. Li, W. Gao, Q. He, L. Zhang, J. Wang, *Adv. Funct. Mater.* **2015**, *25*, 3881.
- [8] C. Chen, E. Karshalev, J. Li, F. Soto, R. Castillo, I. Campos, F. Mou, J. Guan, J. Wang, *ACS Nano* **2016**, *10*, 10389.
- [9] Y. Sun, M. Li, R. Duan, D. Zhang, H. Zhang, B. Song, B. Dong, *Adv. Mater. Technol.* **2018**, *3*, 1800208.
- [10] J. Li, S. Thamphiwatana, W. Liu, B. Esteban-Fernández de Ávila, P. Angsantikul, E. Sandraz, J. Wang, T. Xu, F. Soto, V. Ramez, X. Wang, W. Gao, L. Zhang, J. Wang, *ACS Nano* **2016**, *10*, 9536.
- [11] B. Esteban-Fernández de Ávila, P. Angsantikul, J. Li, M. A. Lopez-Ramirez, D. E. Ramírez-Herrera, S. Thamphiwatana, C. Chen, J. Delezuk, R. Samakapiruk, V. Ramez, M. Obonyo, L. Zhang, J. Wang, *Nat. Commun.* **2017**, *8*, 272.
- [12] X. Wei, M. Beltrán-Gastélum, E. Karshalev, B. Esteban-Fernandez de Avila, J. Zhou, D. Ran, P. Angsantikul, R. H. Fang, J. Wang, L. Zhang, *Nano Lett.* **2019**, *19*, 1914.
- [13] E. Karshalev, B. Esteban-Fernández de Ávila, M. Beltrán-Gastélum, P. Angsantikul, S. Tang, R. Mundaca-Uribe, F. Zhang, J. Zhao, L. Zhang, J. Wang, *ACS Nano* **2018**, *12*, 8397.
- [14] B. Esteban-Fernandez de Avila, W. Gao, E. Karshalev, L. Zhang, J. Wang, *Acc. Chem. Res.* **2018**, *51*, 1901.
- [15] V. Magdanz, S. Sanchez, O. G. Schmidt, *Adv. Mater.* **2013**, *25*, 6581.
- [16] B.-W. Park, J. Zhuang, O. Yasa, M. Sitti, *ACS Nano* **2017**, *11*, 8910.
- [17] B. J. Williams, S. V. Anand, J. Rajagopalan, M. T. Saif, *Nat. Commun.* **2014**, *5*, 3081.
- [18] J. Shao, M. Xuan, H. Zhang, X. Lin, Z. Wu, Q. He, *Angew. Chem.* **2017**, *129*, 13115.
- [19] J. Shao, M. Abdelghani, G. Shen, S. Cao, D. S. Williams, J. C. Van Hest, *ACS Nano* **2018**, *12*, 4877.
- [20] J. Li, P. Angsantikul, W. Liu, B. Esteban-Fernández de Ávila, X. Chang, E. Sandraz, Y. Liang, S. Zhu, Y. Zhang, C. Chen, W. Gao, L. Zhang, J. Wang, *Adv. Mater.* **2018**, *30*, 1704800.
- [21] M. Hamidi, A. Zarrin, M. Foroozesh, S. Mohammadi-Samani, *J. Controlled Release* **2007**, *118*, 145.
- [22] B. Burke, S. Sumner, N. Maitland, C. Lewis, *J. Leukocyte. Biol.* **2002**, *72*, 417.
- [23] M. Studeny, F. C. Marini, J. L. Dembinski, C. Zompetta, M. Cabreira-Hansen, B. N. Bekele, R. E. Champlin, M. Andreeff, *JNCI J. Natl Cancer Inst.* **2004**, *96*, 1593.
- [24] J. Li, X. Li, T. Luo, R. Wang, C. Liu, S. Chen, D. Li, J. Yue, S.-h. Cheng, D. Sun, *Sci. Rob.* **2018**, *3*, eaat8829.
- [25] Y. Alapan, O. Yasa, O. Schauer, J. Giltinan, A. F. Tabak, V. Sourjik, M. Sitti, *Sci. Rob.* **2018**, *3*, eaar4423.

- [26] Z. Lin, X. Fan, M. Sun, C. Gao, Q. He, H. Xie, *ACS Nano* **2018**, *12*, 2539.
- [27] F. Ginhoux, S. Jung, *Nat. Rev. Immunol.* **2014**, *14*, 392.
- [28] A. M. Friedlander, R. Bhatnagar, S. H. Leppla, L. Johnson, Y. Singh, *Infect. Immun.* **1993**, *61*, 245.
- [29] G. Weiss, U. E. Schaible, *Immunol. Rev.* **2015**, *264*, 182.
- [30] P. Pacheco, D. White, T. Sulcek, *PLoS One* **2013**, *8*, e60989.
- [31] W. Lin, R. T. Wu, T. Wu, T.-O. Khor, H. Wang, A.-N. Kong, *Biochem. Pharmacol.* **2008**, *76*, 967.
- [32] M. J. Sweet, D. A. Hume, *J. Leukocyte Biol.* **1996**, *60*, 8.
- [33] P. S. Tobias, J. Mathison, R. Ulevitch, *J. Biol. Chem.* **1988**, *263*, 13479.